Electrical and magnetic properties of ferritin: electron transport phenomena and electron paramagnetic resonance

Labra Muñoz, J.A.

3

FERRITIN SINGLE-ELECTRON DEVICES

In this chapter, the electrical response of single-ferritin particles at low temperatures is reported. The approach, based on wide (10 μm) and narrow (8-25 nm) self-aligned-nano-gaps devices, facilitates the trapping of single ferritin particles. Below 100 K, the devices are stable to allow the acquisition of reproducible current vs. voltage characteristics. A striking feature of single ferritin particles is that the data is in excellent agreement with the Coulomb blockade model, revealing single-electron tunneling as the main transport mechanism through them.

A ferritin single-electron device is, on one hand, a system for studying the electron transport phenomena in ferritin and therefore it broadens the scarce present knowledge on single ferritin particles: as such single-electron devices could reveal information about ferritin that may be of importance in understanding its role in neurodegenerative diseases. On the other hand it is a basic tool for future bio-based electronics, in particular, for the fabrication of protein-based single-electron transistors.

Parts of this chapter have been published in *Biomolecules* **12**, 705 (2022), by **J. A. Labra-Muñoz**, A. de Reuver, F. Koeleman, M. Huber, and H. S. J van der Zant.

3.1. INTRODUCTION

Ferritin, the iron storage protein, has drawn the attention of the scientific community in recent decades. Its unique structure consists of a spherical shell composed of 24 peptide subunits [1]. In mammals, two types of subunits are present: a heavy (21 kDa) and a light (19 kDa) chains [2]. The heavy chain is responsible for the oxidation of Fe(II) to Fe(III). The light chain fosters nucleation and the storage of Fe(III) as a mineral mixture consisting mainly of ferrihydrite, storing iron in a nontoxic form [1]. Dysfunctional ferritin has been related to neurodegenerative diseases for different reasons. First, it allows unwanted egress of iron from the ferritin, which increases the available amount of free iron that is toxic to cells, causing oxidative stress injury [1, 3]. Second, the ferritin core's composition in the brain of patients affected by these diseases has been found to be altered [4, 5]. The mechanism leading to dysfunctional ferritin remains unclear; therefore, a better understanding of the physical properties of individual ferritin particles is vital.

Published studies on the electrical characterization of ferritin have mostly been performed on ferritin networks and monolayers [6–23]. Almost 20 years ago, Xu *et al.* [7] reported that holoferritin networks, i.e., ferritin with an iron core, are 5–15 times more conductive than the networks of the iron-depleted version, apoferritin [7]. Although Xu *et al.* reported S-shaped current vs. voltage (*IV*) characteristics, other phenomena have been observed, such as switching [10] and negative differential resistance [17]. The charge transport through ferritin monolayers has been studied by Kumar *et al.* [6], who reported different transport mechanisms including direct tunneling, sequential tunneling, and hopping, depending on the ferritin iron content. Ferritin multilayers have been studied as well [20], finding highly correlated electron transport, consistent with electron transport in a quantum dot. Bera *et al.* [14] reported similar *IV*s for six layers of holo- and apoferritin. Targeted applications range from multilayered gate dielectrics [8], to metal-insulator nanocomposites [13], high-efficiency solar energy conversion [11], bio-nanobatteries [12], to p-n junctions [15], among others. From a medical perspective, Holovchenko *et al.* [21] showed that the average conductance of Alzheimer's ferritin networks is about two orders of magnitude lower than that of control ferritin, suggesting the use of ferritin resistance measurements as a diagnostic tool.

Studies focused on the electrical characterization of single ferritin are scarce. These studies are based on either scanning tunneling microscopy (STM) [18, 22, 24] or atomic force microscopy (AFM) [7, 25, 26] and are performed at room- or higher temperatures. Single holoferritin was found to be more conductive than apoferritin by AFM [25], as in networks [7]. In contrast, Rakshit *et al.* [24] obtained similar *IV* characteristics for apo- and holoferritin by STM. In this work, single horse-spleen ferritin particles are studied by trapping them in self-aligned nanogaps and measuring their electronic properties at low temperatures. We find that the devices are unstable at room temperature, but below 100 K they allow for the acquisition of reproducible data that establishes Coulomb blockade as the main transport mechanism through them.

3.2. MATERIALS AND METHODS

3.2.1. FERRITIN CHARACTERIZATION

We used commercial horse-spleen ferritin purchased from Sigma Aldrich. Figure 3.1a shows a schematic representation of ferritin. It consists of a mineral core (in red) surrounded by an organic shell (in green) with an outer diameter of 12 nm, and a shell thickness of 2 nm, approximately. From the same batch used in the conductance measurements, we determined the size distribution of ferritin cores through transmission electron microscopy (TEM); see Fig. 3.1b. The analysis of 1502 particles showed that the cores' size varied from 4 to 8.6 nm, as shown in Fig. 3.1c.

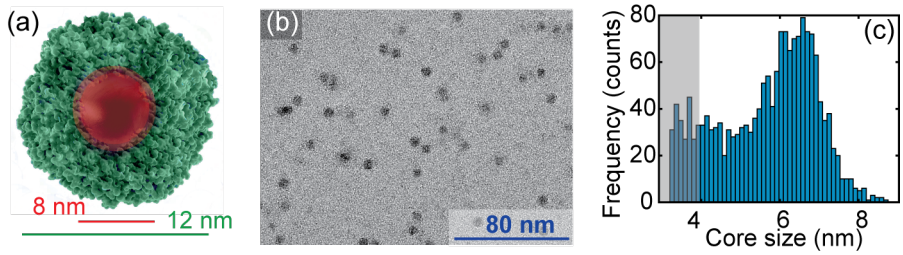

Figure 3.1: (**a**) Schematic representation of ferritin, based on the protein data base (PDB) of horse-spleen apoferritin (PDB ID: 2W0O [27]). The organic shell is in green; the mineral core occupying the internal cavity is in red. (**b**) Transmission electron microscopy (TEM) image of horse-spleen ferritin cores. (**c**) Core-size distribution obtained by the automatic detection of 1502 ferritin cores; the grey-colored area represents the noise region, where it is not possible to discriminate ferritin from image noise. Cores below 4 nm are not accurately identified (gray area).

3.2.2. DEVICE FABRICATION

Self-aligned nanogaps were fabricated following published fabrication routes [28, 29]. Fig. 3.2 shows a scanning electron microscopy image (SEM) of a self-aligned platinum nanogap before ferritin deposition. The distance between the source and drain electrodes (gap length) varied between 8 and 25 nm depending on the fabricated batch, while the gap width was 10 μm.

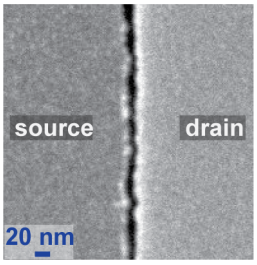

Figure 3.2: Scanning electron microscopy image of an empty device showing a gap of 9−19 nm size between source and drain electrodes.

3.2.3. FERRITIN TRAPPING

Prior to ferritin deposition, we recorded at room temperature and in a vacuum (10^{-4} mbar) the current vs. voltage (*IV*) characteristics of each electrode pair; some samples were also checked at helium temperature. Disregarded were the devices that exhibited a current greater than the noise floor (2 pA) over the bias voltage range probed (±1 V and ±400 mV, for larger (11–25 nm) and smaller gaps (8–13 nm), respectively). Thus, we only selected open gaps for further studies with ferritin particles (see Fig. 3.3b, grey curve).

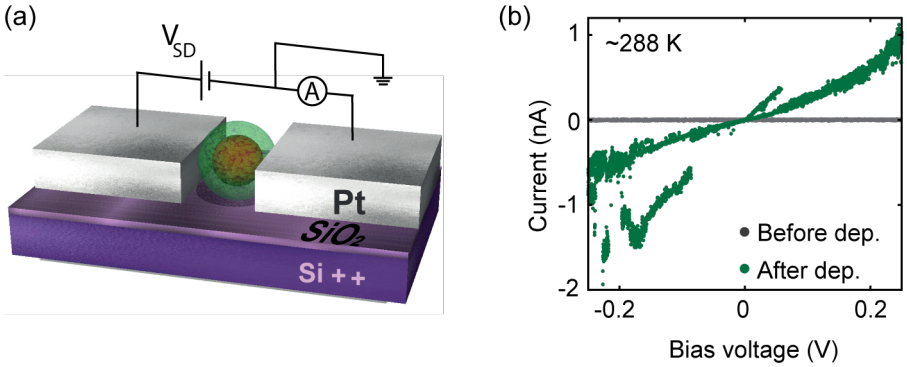

Figure 3.3: (**a**) Schematic circuit of a device containing a ferritin particle. (**b**) Electrical characterization of device A1 before (grey curve) and after (green curve) ferritin deposition, measured at room temperature, in vacuum. The grey curve indicates an open circuit, reflecting an empty device. The increase in current shown in the green curve indicates the capture of ferritin. In both cases, the current is measured by sweeping the voltage from negative to positive values, followed by sweeping from positive to negative values.

The deposition was performed by drop-casting 2–4 μL of a ferritin solution diluted 200 times (~270 μg/mL) onto the electrodes, followed by immediate vacuum pumping. Figure 3.3a shows a schematic representation of a gap after ferritin deposition. We identified the presence of ferritin trapped within the gap by comparing the *IV* characteristics of the gap before and after deposition, measured in vacuum. Figure 3.3b shows representative examples of *IV* curves, measured before (gray curve) and after (green curve) deposition, at room temperature, for device A1. After deposition, a clear increase in current was seen, but the *IV* was unstable with switches between higher and lower conductive states. Furthermore, hysteretic behavior was also often observed while sweeping the bias voltage up and down. This behavior was generally observed for other samples as well.

3.3. RESULTS

The ferritin-deposited devices were cooled down to temperatures close to 4.2 K. At these temperatures, the *IV* characteristics were stable, and the hysteresis was no longer present. Figure A3.9 summarizes the four behaviors detected after ferritin deposition, at temperatures close to 4.2 K. The behaviors were: highly conductive linear *IV*s (most likely ferritin aggregates); still open gaps (no ferritin trapped); tunneling; and Coulomb-blockade

(CB)-like *IV*s. Figure A3.10 shows the reference measurements, using only the buffer solution; after three buffer depositions, no CB-like features were detected.

Here, we focused on analyzing the CB-like *IV* characteristics, since they may represent devices with one particle trapped (see below). Figure 3.4 shows two typical types of CB-like *IV*s recorded at 4.2 or 5 K, displaying clear step-like features (light blue dots) or a single transport gap centered around zero bias (green dots). For clarity and to facilitate the simulations, these *IV* curves were either the descendant curves of the *IV* cycles, i.e., the current recorded from 50 mV to −50 mV, or the ascendant ones. In some cases, abrupt *IV* changes, especially in conductivity, were observed after thermal, voltaic, and

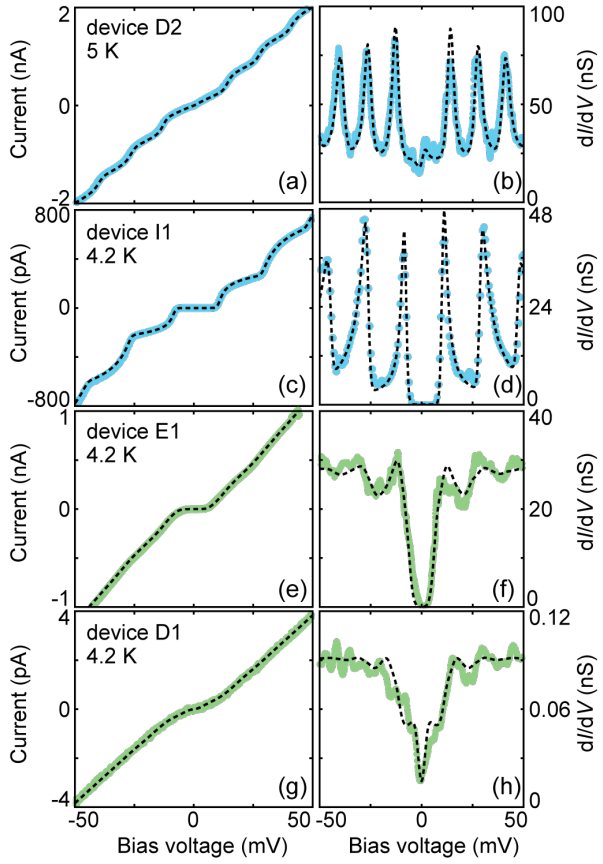

Figure 3.4: Experimental current-voltage (*IV*) characteristics (colored dots) and the corresponding calculated curves using the orthodox Coulomb blockade model (black dashed lines) acquired on four devices, displaying clear step-like features (light blue dots) or a single transport gap centered around zero bias (green dots). (a,e,g) Experimental *IV*s measured on respectively device D2, E1, and D1; obtained by sweeping the voltage from positive to negative values. (c) *IV* measured on device I1; obtained by sweeping the voltage from negative to positive values. The corresponding differential conductance is depicted in figures (b,f,h,d). The data was recorded at either 4.2 or 5.0 K. The parameters used for the simulations are presented in Table 3.1.

temporal cycling. An example of this effect is shown in Fig. 3.4; device D1 (Fig. 3.4g) was recorded first, at 4.2 K. The same device was measured at 5 K again (Fig. 3.4a), after warming it up to 250 K. The current increased by three orders of magnitude, and the IV curve showed clear steps. Next to these changes in device characteristics, abrupt changes in the electrostatic environment are frequently observed. Figure A3.12 in the Appendix illustrates two examples.

We use the orthodox Coulomb Blockade (CB) model [30] to describe the IV characteristics, measured at the lowest recorded temperature as shown in Fig.3.4. The model considers single-electron tunneling, without incorporating second-order processes such as tunneling through virtual states and co-tunneling. A Matlab script was written with R_1, R_2, C_1, C_2, Q_0, T as the simulation parameters; the parameters are defined in the caption of Table 3.1. The temperature is taken to be the measured temperature near the sample and has not been adjusted in the simulations. The black dashed lines shown in Fig. 3.4 are the CB fits to the data; the simulation parameters are listed in Table 3.1. The consistency between the data and simulations is visible both in the IV and the differential conductance ($\mathrm{d}I/\mathrm{d}V$) plots. The excellent agreement indicates that the dominant transport channel is indeed through a single particle although three-terminal measurements with a gate are needed to give a conclusive answer.

Table 3.1: Coulomb-blockade simulation parameters, used to generate the four simulated IVs depicted in Fig. 3.4. C_1 and C_2 are the junction capacitances on the left and right sides, respectively. R_1 and R_2 are the tunnel resistances on the left and right sides, respectively. Q_0 is the offset charge and T is the temperature.

Device	C_1 (aF)	C_2 (aF)	R_1 (MΩ)	R_2 (MΩ)	Q_0 (e)	T (K)
D2	12.0	12.0	0.4	22.0	-0.55	5.0
I1	0.8	8.7	8.6	38.2	-0.06	4.2
E1	9.5	9.2	17.8	17.8	-0.12	4.2
D1	12.0	12.0	5500.0	5500.0	-0.35	4.2

To further investigate the validity of the CB model, we have measured IVs at different temperatures. Figure 3.5 shows IVs obtained at different temperatures, on device A1. At 4.2 K (blue light dots), the IVs present clear Coulomb-blockade steps. At 22 K (orange dots), steps are no longer visible and the blockade part of the IV is linear, i.e., the blockade has been lifted. The black-dashed lines are the Coulomb-blockade fits to the data, using the same simulation parameters R_1, R_2, C_1, C_2, and Q_0 while adjusting only the temperature.

In total 22 devices display Coulomb-blockade like IVs. Figure A3.11 shows the experimental IVs and the CB fits of all data. The simulation parameters are collected in Table A3.10. Figure 3.6 summarizes the total capacitances and resistances used for the simulations.

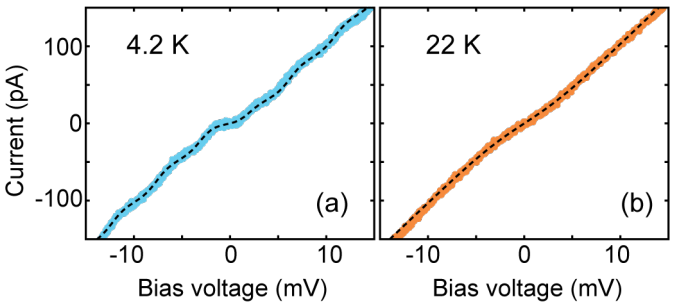

Figure 3.5: Experimental current-voltage characteristics acquired on device A1, at 4.2 K (light blue dots) and 22 K (orange dots). The black dashed lines indicate the calculated curves using the orthodox Coulomb blockade model with parameters: $C_1 = 28$ aF, $C_2 = 34.7$ aF, $R_1 = 0.4$ MΩ, $R_2 = 0.08$ GΩ, $Q_0 = 0.15$e.

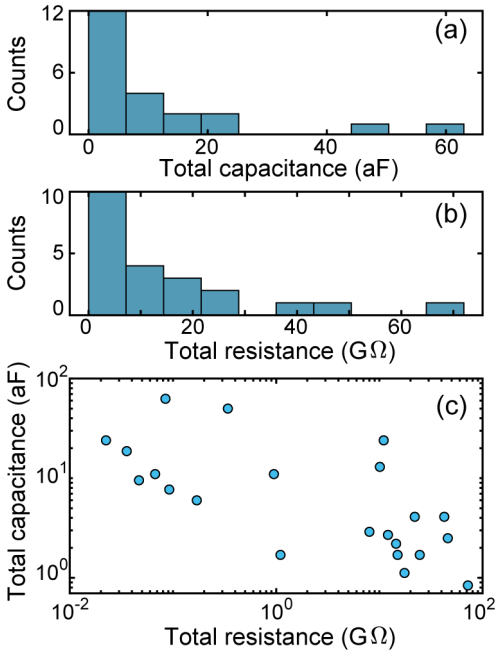

Figure 3.6: Total capacitances ($C = C_1 + C_2$) and total resistances ($R = R_1 + R_2$) calculated with the orthodox Coulomb blockade model for the 22 devices showing Coulomb-blockade at temperatures below 100 K. Table A3.10 contains the entire set of Coulomb blockade parameters used to model each device, at the lowest recorded temperature. (a) Total capacitance histogram. (b) Total resistance histogram. (c) Total capacitance plotted against the total resistance.

A broad dispersion in the parameters is found: the total capacitance varies over two orders of magnitude from 0.84 to 62.7 aF, while the total resistance varies over four orders of magnitude from 0.02 GΩ to 72 GΩ.

3.4. CAPACITANCE AND RESISTANCE ESTIMATIONS

A crude model to estimate the capacitances of ferritin particles is based on two parallel plate capacitors connected between the ferritin mineral core and the two electrodes, on either side (C_1, C_2). These capacitances are expressed as

$$C_{1,2} = \epsilon_r \cdot \epsilon_0 \cdot A/d, \tag{3.1}$$

where ϵ_0 is the vacuum permittivity and ϵ_r is the relative permittivity of the ferritin organic shell. Laghaei *et al.*[31] assigned 20 to the ϵ_r of H-chain ferritin. In addition, Li *et al.*[32] modeled ϵ_r in proteins and established that it varies between 6 and 30, for inner and outer regions of the proteins. For our estimates, we consider ϵ_r to be between 10 and 20. Lastly, A is the contact area, and d is the distance between the plates. The total capacitance is denoted as $C = C_1 + C_2$.

In the Coulomb blockade (CB) model, the resistance (R) of an individual ferritin particle can be considered as composed by two tunnel resistances in series, one from the tunnel barrier between the source electrode and the core, and one tunnel barrier between the core and the drain electrode, i.e., $R = R_1 + R_2$. Each of these resistances can be expressed as

$$R_{1,2} = R_0 \exp(\beta d), \tag{3.2}$$

where R_0 is an effective contact resistance, d is the thickness of the dielectric film (same as in equation 3.1), and β is the exponential distance decay factor.

With these two expressions, we now calculate the capacitances and resistances for 4 different limit cases (see figure 3.7). For simplicity, the ferritin particle is depicted as a cube, but the reasoning is analogous for a spheric particle.

3.4.1. CAPACITANCE ESTIMATES

Case I: symmetric in between the electrodes. This case (Fig. 3.7a) corresponds to the upper bound estimate for the capacitance since it considers the contact area, A, to be maximized (8 x 8 nm^2). d is considered to be the ferritin shell thickness ($d_s \sim 2$ nm). The capacitance estimates are shown in table 3.2.

A (nm^2)	d (nm)	ϵ_r	C (aF)
8 x 8	2	10	5.7
8 x 8	2	20	11.3

Table 3.2: Total capacitance values (C) estimated by assuming a parallel plate capacitor model, for case I. $C = C_1 + C_2$ with $C_1 = C_2$ and $d = d_s$.

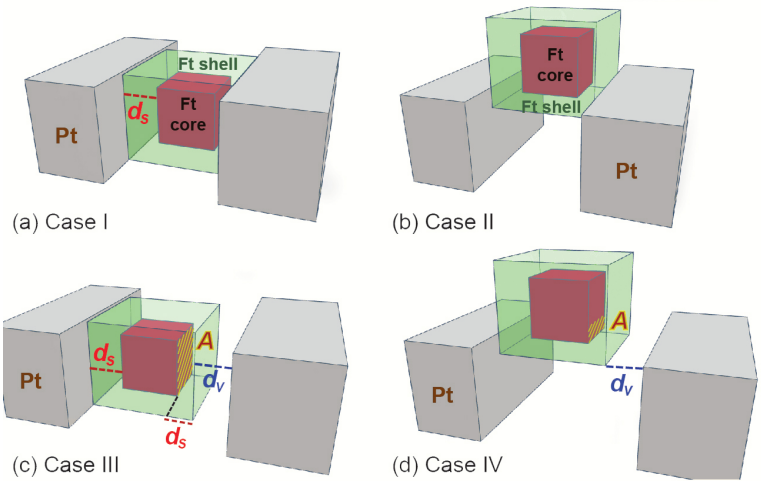

Figure 3.7: Schematic of the limiting cases of the ferritin parallel plate capacitor (C) and resistance (R) estimates. The contact area, the protein shell thickness and the vacuum distance are represented by the letters A, d_s, d_v, respectively. (a) Case I: the ferritin particle is connected symmetrically to both electrodes while maximizing the contact area. (b) Case II: ferritin is symmetrically connected to the electrodes while minimizing the contact area. (c) Case III: the ferritin particle is connected asymmetrically to both electrodes (vacuum space in between) while maximizing the contact area. (d) Case IV: the ferritin particle is connected asymmetrically to both electrodes (vacuum space in between) while minimizing the contact area.

Case II: symmetric on top of the electrodes. In this scenario (Fig. 3.7b), the ferritin particle is no longer in between the electrodes, but rather on top of them. This results in A being small and we take 1 x 8 nm^2 as the minimal area; d is the thickness of the ferritin shell (~2 nm). The total estimated capacitances are shown in table 3.3.

A (nm^2)	d (nm)	ϵ_r	C (aF)
1 x 8	2	10	0.71
1 x 8	2	20	1.42

Table 3.3: Total capacitance values (C) estimated by assuming a parallel plate capacitor model, for case II. $C = C_1 + C_2$ with $C_1 = C_2$ and $d = d_s$.

Case III: asymmetric in between the electrodes. In this situation (Fig. 3.7c), the gap between the electrodes is bigger than the ferritin size, resulting in an asymmetric coupling to the electrodes. One side of the ferritin particle makes contact with one of the electrodes, but there is some space in between the particle and the other electrode. The capacitance of the latter side of the ferritin (C_2) can be estimated by considering a parallel plate capacitor made of two different dielectrics (the ferritin shell and vacuum), which is effectively two capacitors in series of capacitances $\epsilon_r \epsilon_0 A/d_s$ and $\epsilon_0 A/d_v$, expressed as

$$C_2 = \frac{\epsilon_r \epsilon_0 A}{d_s + \epsilon_r d_v}, \tag{3.3}$$

where d_v is the distance between the ferritin shell and the electrode. Table 3.4 shows the estimated capacitances.

A (nm^2)	d_s (nm)	d_v (nm)	ϵ_r	C_1 (aF)	C_2 (aF)	C (aF)
8 x 8	2	1	10	2.8	0.5	3.3
8 x 8	2	1.5	10	2.8	0.4	3.2
8 x 8	2	1	20	5.7	0.5	6.2
8 x 8	2	1.5	20	5.7	0.3	6.0

Table 3.4: Total capacitance values (C) estimated by assuming a parallel plate capacitor model, for case III. $C = C_1 + C_2$ with $C_1 > C_2$.

Case IV: asymmetric on top of the electrodes. In this case (Fig. 3.7d), the ferritin particle is on top of one electrode (as in case II), but there is a space between the particle and the other electrode (asymmetric barriers) as in case III. To estimate the total capacitance we can combine the strategies followed in cases II (A = 1 x 8 nm^2) and III. The estimated capacitances are shown in table 3.5.

A (nm^2)	d_s (nm)	d_v (nm)	ϵ_r	C_1 (aF)	C_2 (aF)	C (aF)
1 x 8	2	1	10	0.35	0.06	0.41
1 x 8	2	1.5	10	0.35	0.05	0.40
1 x 8	2	1	20	0.7	0.07	0.77
1 x 8	2	1.5	20	0.7	0.05	0.75

Table 3.5: Total capacitance values (C) estimated by assuming a parallel plate capacitor model, for case IV. $C = C_1 + C_2$ with $C_1 > C_2$.

3.4.2. RESISTANCE ESTIMATES

β-decay [1] values, at 80 K for different proteins, have been reported to vary from 0.19 Å^{-1} (holo-azurin) to 0.33 Å^{-1} (apo-azurin: azurin without Cu) [33]. For our estimates, we consider the average value of β = 0.26 Å^{-1}. To estimate the contact resistance we use the results of a measurement on a single (holo)azurin. A resistance value of 1.8 GΩ has been reported for this protein [33]. Considering a contact area of 9 nm^2, a length of 3.3 nm [33], and a β of 0.19 Å^{-1} in equation 3.2, the contact resistance (R_0) equals 3.4 MΩ. We assume that the contact resistance is inversely proportional to the contact area, so the contact resistance per nm^2 is R_0^* = 30.6 MΩ· nm^2. With these numbers for β and R_0^* we now calculate the resistance values for the four cases considered before.

[1] Exponential distance decay factor.

Case I: symmetric in between the electrodes. This case (Fig. 3.7a) corresponds to the lower bound estimate of the total resistance, where A is considered to be 8 x 8 nm^2; therefore R_0 = 0.48 MΩ. The resistances are symmetric, i.e., $R_1 = R_2$. The total resistance $R = R_1 + R_2$ is shown in table 3.6.

A (nm^2)	R_0 (MΩ)	β (Å^{-1})	R (GΩ)
8 x 8	0.48	0.26	0.17

Table 3.6: Resistance values estimated assuming two tunnel resistances in series, for case I. $R = R_1 + R_2$, with $R_1 = R_2$.

Case II: symmetric on top of the electrodes. In this case (Fig. 3.7b), the contact area A is minimum (1 x 8 nm^2), therefore R_0 = 3.83 MΩ. The estimated resistances for this scenario are depicted in table 3.7.

A (nm^2)	R_0 (MΩ)	β (Å^{-1})	R (GΩ)
1 x 8	3.83	0.26	1.39

Table 3.7: Resistance values estimated assuming two tunnel resistances in series, for case II. $R = R_1 + R_2$, with $R_1 = R_2$.

Case III: asymmetric in between the electrodes. In this situation (Fig. 3.7c), the gap between the electrodes is bigger than the ferritin size, resulting in extra space between the ferritin and one of the electrodes. We can consider this extra space (d_v) as a third tunnel resistance (in vacuum) connected in series to the others. For simplicity, the vacuum space is considered as a prolongation of the ferritin shell, i.e., it exhibits the same $\beta-$decay parameter. This estimation yields a resistance that is smaller than it would be if vacuum was considered, with a barrier given by the work function of platinum of 5.6 eV [34]. The resistance estimates are depicted in Table 3.8.

A (nm^2)	R_0 (MΩ)	β (Å^{-1})	d_v(nm)	R_1 (GΩ)	R_2 (GΩ)	R (GΩ)
8 x 8	0.48	0.26	1	0.09	1.17	1.26
8 x 8	0.48	0.26	1.5	0.09	4.30	4.39
8 x 8	0.48	0.26	2	0.09	15.77	15.86

Table 3.8: Resistance values estimated assuming two tunnel resistances in series, for case III. $R = R_1 + R_2$, with R_1 the resistance due to the protein shell only; R_2 is the resistance due to the protein shell and the vacuum space, considered as an extension of the organic shell.

Case IV: asymmetric on top of the electrodes. This scenario (Fig. 3.7d) is a combination of cases II and III, i.e., the contact area is minimum (1 x 8 nm^2), and the vacuum space is treated as a prolongation of the organic protein barrier (d_v). The total resistance estimates are presented in table 3.9.

A (nm^2)	R_0 (MΩ)	β (Å^{-1})	d_v(nm)	R_1 (GΩ)	R_2 (GΩ)	R (GΩ)
1 x 8	3.83	0.26	1	0.70	9.35	10.05
1 x 8	3.83	0.26	1.5	0.70	34.30	35.00
1 x 8	3.83	0.26	2	0.70	125.85	126.55

Table 3.9: Resistance values estimated assuming two tunnel resistances in series, for case IV. $R = R_1 + R_2$, with R_1 the resistance due to the protein shell only; R_2 is the resistance due to the protein shell and the vacuum space, considered as an extension of the organic shell.

3.5. DISCUSSIONS

Considering the four different cases, the ratio between the minimum and maximum estimated capacitances (C_{min} = 0.4 aF; C_{max} = 11.3 aF) is 0.035 when taking the variation of ϵ_r between 10 and 20 into account. From the Coulomb blockade (CB) fits to the experimental data, C_{min}/C_{max} is 0.01, which is somewhat lower than our estimate. The maximum estimated capacitances (5.7 and 11.3 aF) are about 5 times lower than the maximum experimental capacitance (62.7 aF). A possible explanation to account for this difference is to consider a barrier thickness thinner than 2 nm. From TEM images we obtained a protein shell size distribution centered around 12 nm, with variations from 10 to 14 nm, i.e., thickness variations of ±1 nm were detected. The maximum capacitance (case I) obtained for a shell thickness of 1 nm is 22.6 aF, which is 2.7 times lower than the maximum experimental capacitance. Another aspect to consider is that our assumed dielectric constant might be different for ferritin. It has been reported that ϵ_r can be 80 for aqueous regions close to ferritin [32]. If we consider the previous example, but with ϵ_r = 55 instead, a maximum capacitance of 62.3 aF is obtained. Note that only 2 out of 22 experimental capacitances are greater than 24 aF, so these cases are rather isolated events.

The ratio between the minimum and maximum estimated resistances (R_{min}/R_{max}) is 10^{-3}. From the CB fits to the experimental data, R_{min}/R_{max} is $2 \cdot 10^{-4}$, which is a factor of 5 lower. The maximum experimental resistance is within the range of our estimates. However, the minimum experimental resistance (0.02 GΩ) is lower than our minimum estimate (0.17 GΩ). One possible reason is that β is smaller than what we assumed. For example, if we consider β = 0.21 Å^{-1} instead, R_{min} (case I) is 0.06 GΩ, which is in the same order of magnitude as the smaller experimental resistance.

In conclusion, we demonstrated that individual ferritin particles can be trapped in self-aligned nanogaps. The observed instability at room temperature was suppressed at low temperatures, and clear Coulomb blockade effects were observed including Coulomb staircases. Excellent fits of the current–voltage characteristics to the Coulomb blockade model strongly indicate that transport is through an individual particle. Estimates based on different arrangements of the particle in between the electrodes and reported values for transport through proteins reproduced the capacitance and resistance values determined from the CB model. Thus, the experiments showed that ferritin particles act as a model CB system, and in the next step, it would be interesting to relate the transport characteristics to specific ferritin properties.

3.6. APPENDIX

3.6.1. FERRITIN PURITY ASSESSMENT

Commercial horse-spleen ferritin purchased from Sigma Aldrich (Cat.No. 270-40, Lot: 08E1805) of 54 mg/ml protein concentration was used with no further purification. For the conductance measurements, the ferritin solution was diluted by a factor of 200 using a buffer solution (0.15 M NaCl and 10 mM Tris, pH 8.0, 0.1% sodium azide). The final solution has a protein concentration of 270 μg/ml with >95% purity as assessed by sodium dodecyl sulfate–polyacrylamide gel electrophoresis (SDS-PAGE, see Fig. A3.8c). The strong presence of ferritin monomers is detected (strong band around 500 kDa). A less intense band of multimers or ferritin aggregates is detected as well (weaker bands around 1000-1200 kDa). Dynamic light scattering (DLS) confirms these findings and shows the peak of greatest intensity centered around 12 nm (Fig. A3.8a). Two other peaks are present, centered at 265 and 2780 nm, and attributed to the appearance of contaminants when handling the sample, e.g., dust. Note, that these 2 peaks have a mass that is smaller than 0.5% of the total mass, which indicates that more than 99.5% of the total mass is attributed to ferritin (single particles and aggregates).

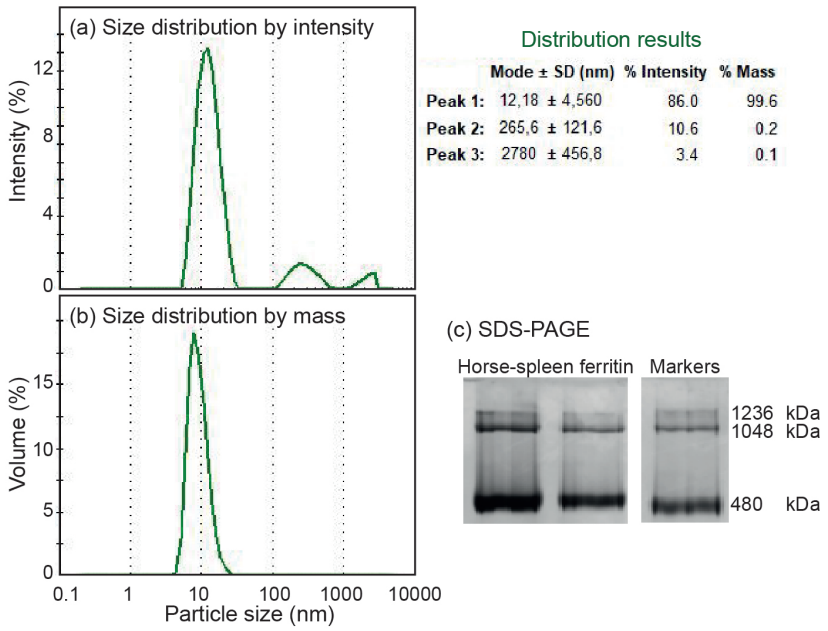

Figure A3.8: Purity assessment of horse-spleen ferritin. (a,b) Dynamic light scattering showing the particle size distribution: one main Gaussian peak with μ=12.2 nm and σ=4.5 nm. (c) Non-denaturing polyacrylamide gel electrophoresis of horse-spleen ferritin stained with Coomassie. The strong band of 500 kDa agrees with ferritin monomers (24-mer protein) while the weaker bands of 1048 and 1236 kDa correspond to ferritin multimers (dimers/trimers) or aggregates of ferritin protein. Markers refer to NativeMark Unstained Protein Standard (Cat. No. LC0725).

3.6.2. *IV* TYPES (LOW TEMPERATURE)

After ferritin deposition, four different IV curve types were obtained, shown in Fig. A3.9. Normally, around 90-95 % devices remained open (red dots; panel (a)); 0-10 % devices show a conductive linear behavior (green dots; panel (a)); 3-8 % show Coulomb-blockade-like features (blue dots; panel (b)); some devices (0-1 %) show tunneling-like IV characteristics (purple dots; panel (c)).

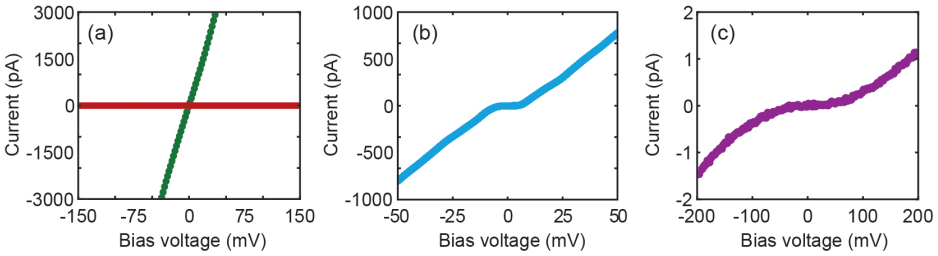

Figure A3.9: Examples of the four types of experimental current-voltage (IV) characteristics measured after deposition of ferritin at 4.2 K; IVs are recorded by sweeping the voltage from negative to positive values, and vice versa. Note, the absence of hysteresis. (a) Device that remains open (red dots) and a device that shows a highly conductive linear behavior (green dots). (b) Device that shows Coulomb-blockade-like features. (c) Device that shows tunnelling-like behavior.

3.6.3. REFERENCE MEASUREMENTS

Reference measurements, acquired at 4.2 K with the buffer solution without ferritin (see Ferritin purity assessment) were also performed. The buffer was deposited on two different chips (A, B) and $3-4$ μl of buffer was deposited three times on each device. After the 3^{rd} buffer deposition, 100% of devices from chip A (5 devices) and 77% of the devices from chip B (10 devices) remained open (red dots). The 33% of the devices on chip B show either tunneling (purple dots, 2 devices) or linear behavior (green dots, 1 device). No Coulomb-blockade-like IVs were measured in any device on either chip.

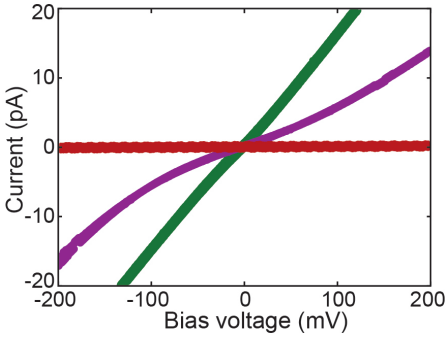

Figure A3.10: Current-voltage (IV) characteristics measured after deposition of buffer without ferritin, at 4.2 K. Three different IV types are observed: device that remains open (red dots), tunneling-like (purple dots), linear behavior (green dots).

3.6.4. CB EXPERIMENTAL DATA AND FITS

22 different devices showing CB-like features were measured (blue dots, Fig. A3.11). For all of them, CB fits were performed (black dashed lines), by using the parameters that are shown in table A3.10. The name of a device is composed of a letter and a number. The letter indicates a specific electrode pair of a chip (source-gap-drain). The number refers to the CB version that was detected: in some cases, an abrupt change in the IV shape and specifically in the conductivity was detected after any of the following 3 processes:

- thermal cycle: warming it up until 250 K and then cooling it down again to 4.2 K;
- voltaic cycle: after applying more than 0.5 V;
- temporal cycle: random spontaneous change, e.g., hours, days, or after 2 weeks.

This means that devices D1 and D2 are two different CB realizations measured with the same electrode pair.

Table A3.10: Coulomb blockade simulations parameters, used to generate the 22 simulated IVs depicted in Fig. A3.11. C_1 and C_2 are the junction tunnel capacitances on the left and right sides, respectively. R_1 and R_2 are the tunnel resistances on the left and right sides, respectively. Q_0 is the offset charge. T is the temperature, taken to be the temperature measured near the sample.

Device	C_1 (aF)	C_2 (aF)	R_1 (GΩ)	R_2 (GΩ)	Q_0 (e)	T (K)
A1	28.0	34.7	0.0004	0.084	0.15	4.2
B1	20.0	30.0	0.2	0.14	-0.15	4.2
C1	1.1	1.1	7.5	7.0	0.24	80.0
D1	12.0	12.0	5.5	5.5	-0.35	4.2
D2	12.0	12.0	0.00042	0.022	-0.545	5.0
E1	9.5	9.2	0.0178	0.0178	-0.12	4.2
E2	4.5	6.5	0.65	0.3	-0.2	5.0
E3	6.5	4.5	0.0031	0.064	-0.15	4.2
F1	4.3	3.4	0.04	0.052	0.75	5.0
G1	0.42	0.42	37.0	35.0	0.08	16.0
H1	0.8	1.7	22.0	24.0	-0.01	0.8
I1	0.8	8.73	0.0086	0.0382	-0.062	4.2
J1	2.6	1.5	15.0	7.0	0.37	1.8
J2	2.6	1.5	32.0	10.5	0.05	1.8
K1	0.17	0.95	7.7	9.8	0.3	3.0
L1	0.7	1.0	4.8	19.8	0.3	4.5
M1	1.2	1.5	8.3	3.8	-0.22	4.5
M2	6.0	7.0	4.5	5.6	-0.37	4.2
N1	0.7	1.0	0.6	0.5	0.05	4.2
O1	3.0	3.0	0.09	0.08	-0.15	4.2
O2	1.1	1.8	4.0	4.0	0.03	4.2
P1	0.5	1.2	10.0	5.0	0.16	4.2

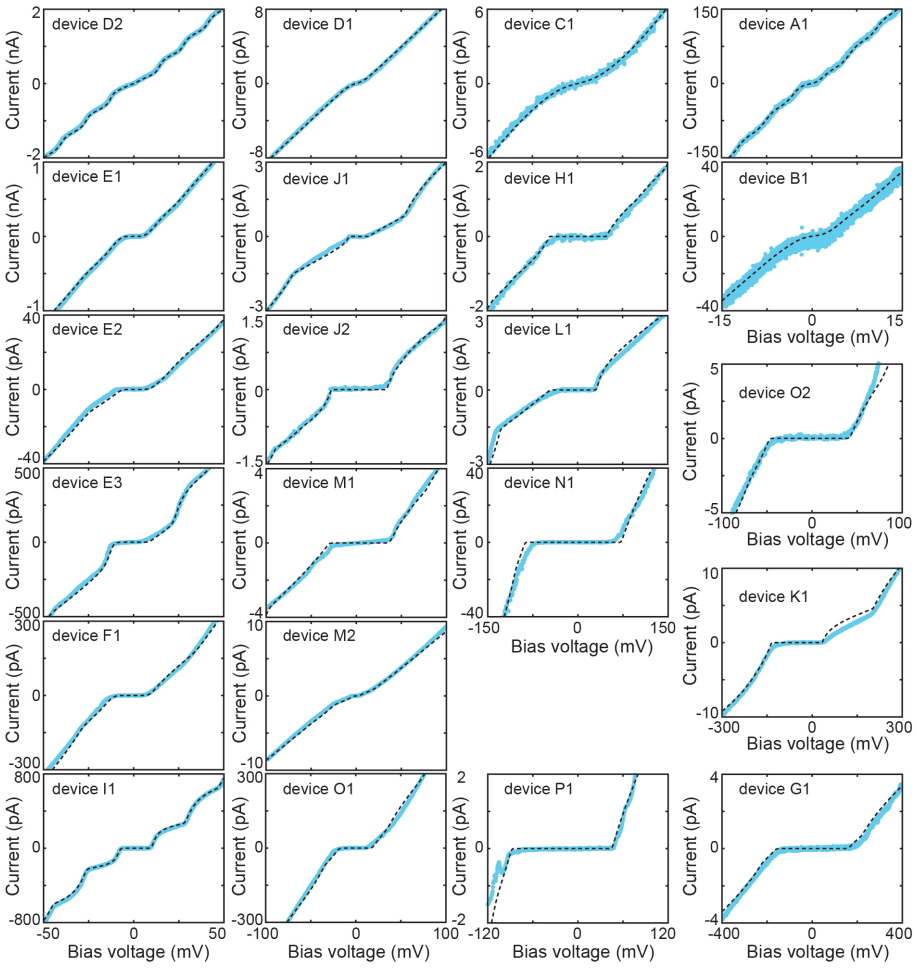

Figure A3.11: Low-temperature experimental current-voltage characteristics (blue dots) and the corresponding calculated curves using the orthodox Coulomb blockade model (black dashed lines) acquired on the 22 devices displaying Coulomb blockade-like features. The fit parameters and the temperature at which the measurement was performed are collected in Table A3.10.

3.6.5. CHARGE OFFSET VARIATIONS

All 22 devices showed charge offset, Q_0, changes. In some cases, this occurred after a day of stable measurements, in other devices this happened within a day or a few hours. Figure A3.12 shows two different devices displaying Q_0 changes within the same day.

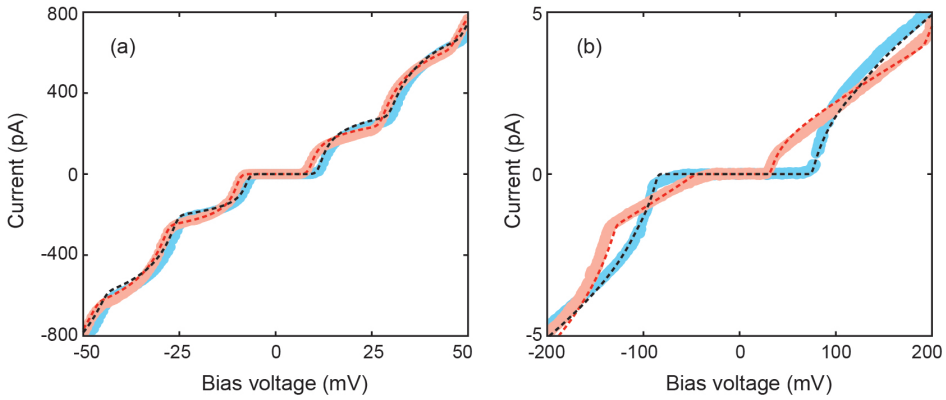

Figure A3.12: Experimental current-voltage (IV) characteristics (colored dots) and the corresponding calculated curves using the Coulomb blockade model (dashed lines) acquired on the same device, at different times (same day). (a) Device I1: Q_0 changes from 0.02e (red curve) to -0.11e (blue curve). The other parameters are the same for both curves and can be found in Table A3.10. (b) Device L1, Q_0 changes from 0.3e (red curve) to 0.03e (blue curve). The other parameters can be found in table A3.10.

3.6.6. ROOM TEMPERATURE MEASUREMENTS

After deposition, the devices in which ferritin was trapped presented a clear increase in current, the IV was unstable with switches between higher and lower conductive states. In addition, hysteretic behavior was observed while sweeping the bias voltage up and down. Figure A3.13 shows two examples in addition to the one shown in fig. 3.3b.

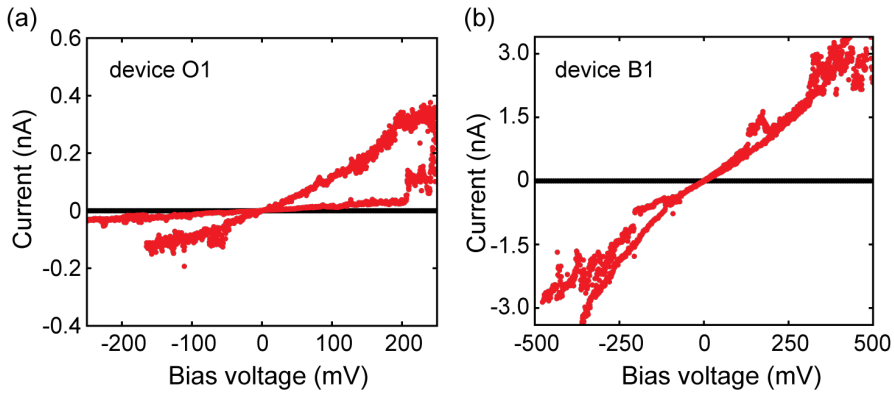

Figure A3.13: Experimental current-voltage (IV) characteristics before (in black) and after ferritin deposition (in red), performed at room temperature, in vacuum, on two different devices.

REFERENCES

[1] P. Arosio, L. Elia, and M. Poli, *Ferritin, cellular iron storage and regulation,* IUBMB Life **69**, 414 (2017).

[2] D. Finazzi and P. Arosio, *Biology of ferritin in mammals: an update on iron storage, oxidative damage and neurodegeneration,* Archives of toxicology **88**, 1787 (2014).

[3] A. Friedman, P. Arosio, D. Finazzi, D. Koziorowski, and J. Galazka-Friedman, *Ferritin as an important player in neurodegeneration,* Parkinsonism and Related Disorders **17**, 423 (2011).

[4] C. Quintana, S. Bellefqih, J. Laval, J.-L. Guerquin-Kern, W. Ting-Di, J. Avila, I. Ferrer, R. Arranz, and C. Patiño, *Study of the localization of iron, ferritin, and hemosiderin in alzheimer's disease hippocampus by analytical microscopy at the subcellular level,* Journal of structural biology **153**, 42 (2006).

[5] C. Quintana and L. Gutiérrez, *Could a dysfunction of ferritin be a determinant factor in the aetiology of some neurodegenerative diseases?* Biochimica et Biophysica Acta (BBA) - General Subjects **1800**, 770 (2010).

[6] K. S. Kumar, R. R. Pasula, S. Lim, and C. A. Nijhuis, *Long-range tunneling processes across ferritin-based junctions,* Advanced Materials **28**, 1824 (2016).

[7] D. Xu, G. D. Watt, J. N. Harb, and R. C. Davis, *Electrical conductivity of ferritin proteins by conductive afm,* Nano Letters **5**, 571 (2005).

[8] B. J. Kim, Y. Ko, J. H. Cho, and J. Cho, *Organic field-effect transistor memory devices using discrete ferritin nanoparticle-based gate dielectrics,* Small **9**, 3784 (2013).

[9] S.-I. Yamamoto, K. Kobayashi, H. Yamada, H. Yoshioka, Y. Uraoka, T. Fuyuki, and I. Yamashita, *Electrical characterisitics of ferritin cores investegated by kelvin probe force microscopy,* Journal of Physics: Conference Series **100**, 052004 (2008).

[10] C. Zhang, J. Shang, W. Xue, H. Tan, L. Pan, X. Yang, S. Guo, J. Hao, G. Liu, and R.-W. Li, *Convertible resistive switching characteristics between memory switching and threshold switching in a single ferritin-based memristor,* Chem. Commun. **52**, 4828 (2016).

[11] S. Erickson, T. Smith, L. Moses, R. Watt, and J. Colton, *Non-native co-, mn-, and ti-oxyhydroxide nanocrystals in ferritin for high efficiency solar energy conversion,* Nanotechnology **26**, 015703 (2015).

[12] G. Watt, J.-W. Kim, B. Zhang, T. Miller, J. Harb, R. Davis, and S. Choi, *A protein-based ferritin bio-nanobattery,* Journal of Nanotechnology **2012**, 516309 (2012).

[13] S. Bera, J. Kolay, S. Banerjee, and R. Mukhopadhyay, *Nanoscale on-silico electron transport via ferritins,* Langmuir **33**, 1951 (2017).

[14] S. Bera, J. Kolay, P. Pramanik, A. Bhattacharyya, and R. Mukhopadhyay, *Long-range solid-state electron transport through ferritin multilayers,* J. Mater. Chem. C **7**, 9038 (2019).

[15] Y. Mulyana, M. Uenuma, N. Okamoto, Y. Ishikawa, I. Yamashita, and Y. Uraoka, *Creating reversible p–n junction on graphene through ferritin adsorption,* ACS Applied Materials & Interfaces **8**, 8192 (2016).

[16] H. J. Shin, K. M. Shin, J. W. Lee, C. H. Kwon, S.-H. Lee, S. I. Kim, J.-H. Jeon, and S. J. Kim, *Electrocatalytic characteristics of electrodes based on ferritin/carbon nanotube composites for biofuel cells,* Sensors and Actuators B: Chemical **160**, 384 (2011).

[17] J. Kolay, S. Bera, T. Rakshit, and R. Mukhopadhyay, *Negative differential resistance behavior of the iron storage protein ferritin,* Langmuir **34**, 3126 (2018).

[18] T. Rakshit and R. Mukhopadhyay, *Tuning band gap of holoferritin by metal core reconstitution with cu, co, and mn,* Langmuir **27**, 9681 (2011).

[19] T. Rakshit, S. Bera, J. Kolay, and R. Mukhopadhyay, *Nanoscale solid-state electron transport via ferritin: Implications in molecular bioelectronics,* Nano-Structures & Nano-Objects **24**, 100582 (2020).

[20] C. Rourk, Y. Huang, M. Chen, and C. Shen, *Indication of strongly correlated electron transport and mott insulator in disordered multilayer ferritin structures (dmfs),* Materials (Basel) **14**, 4527 (2021).

[21] A. Holovchenko, *Electrical Characterization of Nanoparticle and Protein Networks.*, Ph.D. thesis, Delft University of Technology, July 04 (2017).

[22] M. Preisinger, M. Krispin, T. Rudolf, S. Horn, and D. Strongin, *Electronic structure of nanoscale iron oxide particles measured by scanning tunneling and photoelectron spectroscopies,* Physical Review B **71**, 165409 (2005).

[23] S. Kumagai, S. Yoshii, N. Matsukawa, K. Nishio, R. Tsukamoto, and I. Yamashita, *Self-aligned placement of biologically synthesized coulomb islands within nanogap electrodes for single electron transistor,* Applied Physics Letters **94**, 083103 (2009).

[24] T. Rakshit, S. Banerjee, and R. Mukhopadhyay, *Near-metallic behavior of warm holoferritin molecules on a gold(111) surface,* Langmuir **26**, 16005 (2010).

[25] T. Rakshit, *Differentiating holo- and apoferritin by afm approach,* Journal of Surface Science and Technology **31**, 165 (2015).

[26] S. H. Choi, J.-W. Kim, S.-H. Chu, Y. Park, G. C. King, P. T. Lillehei, S.-J. Kim, and J. R. Elliott, *Ferritin-templated quantum dots for quantum logic gates,* in *Smart Structures and Materials 2005: Smart Electronics, MEMS, BioMEMS, and Nanotechnology*, Vol. 5763, edited by V. K. Varadan, International Society for Optics and Photonics (SPIE, 2005) pp. 213 – 232.

[27] N. de Val, J.-P. Declercq, C. K. Lim, and R. R. Crichton, *Structural analysis of haemin demetallation by l-chain apoferritins,* Journal of Inorganic Biochemistry **112**, 77 (2012).

[28] A. Fursina, S. Lee, R. G. S. Sofin, I. V. Shvets, and D. Natelson, *Nanogaps with very large aspect ratios for electrical measurements,* Applied Physics Letters **92**, 113102 (2008).

[29] J. Labra-Muñoz, Z. Konstantinović, L. Balcells, A. Pomar, H. S. J. van der Zant, and D. Dulić, *Trapping and electrical characterization of single core/shell iron-based nanoparticles in self-aligned nanogaps,* Applied Physics Letters **115**, 063104 (2019).

[30] T. Claeson, P. Delsing, D. Haviland, L. Kuzmin, and K. K. Likharev, *Correlated single electron tunneling in ultrasmall junctions,* in *Nonlinear Superconductive Electronics and Josephson Devices*, edited by G. Costabile, S. Pagano, N. F. Pedersen, and M. Russo (Springer US, Boston, MA, 1991) pp. 197–228.

[31] R. Laghaei, W. Kowallis, D. G. Evans, and R. D. Coalson, *Calculation of iron transport through human h-chain ferritin,* The Journal of Physical Chemistry A **118**, 7442 (2014).

[32] L. Li, C. Li, Z. Zhang, and E. Alexov, *On the 'dielectric "constant" of proteins: Smooth dielectric function for macromolecular modeling and its implementation in delphi,* Journal of chemical theory and computation **9**, 2126 (2013).

[33] N. Amdursky, D. Marchak, L. Sepunaru, I. Pecht, M. Sheves, and D. Cahen, *Electronic transport via proteins,* Advanced Materials **26**, 7142 (2014).

[34] N. Ibrahim, D. Poulidi, M. E. Rivas, I. D. Baikie, and I. S. Metcalfe, *The role of sodium surface species on oxygen charge transfer in the pt/ysz system,* Electrochimica Acta **76**, 112 (2012).